




A nonnatural peptide targeting the A-kinase anchoring function of PI3K γ for therapeutic cAMP modulation in pulmonary cells

Received for publication, April 12, 2024, and in revised form, September 10, 2024. Published, Papers in Press, October 10, 2024.

<https://doi.org/10.1016/j.jbc.2024.107873>

Angela Della Sala¹, Laura Tasca^{1,2}, Cosmin Butnaru¹ , Valentina Sala^{1,2} , Giulia Prono¹ , Alessandra Murabito¹, Olga Valentina Garbero¹ , Enrico Millo³, Leonardo Terranova^{4,5} , Francesco Blasi^{4,6}, Andrea Gramegna^{4,6}, Stefano Aliberti⁷, Alberto Massarotti⁸, Sonja Visentin¹, Emilio Hirsch^{1,2} , and Alessandra Ghigo^{1,2,*}

From the ¹Department of Molecular Biotechnology and Health Sciences, Molecular Biotechnology Center "Guido Tarone", University of Torino, Torino, Italy; ²Kither Biotech Srl, Torino, Italy; ³Section of Biochemistry, Department of Experimental Medicine, University of Genova, Genova, Italy; ⁴Internal Medicine Department, Respiratory Unit and Cystic Fibrosis Center, Fondazione IRCCS Ca' Granda Ospedale Policlinico, Milan, Italy; ⁵Microbiology and Virology Specialization School, University of Pavia, Pavia, Italy; ⁶Department of Pathophysiology and Transplantation, University of Milan, Milan, Italy; ⁷Respiratory Unit, IRCCS Humanitas Research Hospital, Humanitas University, Milan, Italy; ⁸Department of Pharmaceutical Science, University of Piemonte Orientale, Novara, Italy

Reviewed by members of the JBC Editorial Board. Edited by Philip A. Cole

A-kinase anchoring proteins (AKAPs) are key orchestrators of cAMP signaling that act by recruiting protein kinase A (PKA) in proximity of its substrates and regulators to specific subcellular compartments. Modulation of AKAPs function offers the opportunity to achieve compartment-restricted modulation of the cAMP/PKA axis, paving the way to new targeted treatments. For instance, blocking the AKAP activity of phosphoinositide 3-kinase γ (PI3K γ) improves lung function by inducing cAMP-mediated bronchorelaxation, ion transport, and antiinflammatory responses. Here, we report the generation of a nonnatural peptide, D-retroinverso (DRI)-Pep #20, optimized to disrupt the AKAP function of PI3K γ . DRI-Pep #20 mimicked the native interaction between the N-terminal domain of PI3K γ and PKA, demonstrating nanomolar affinity for PKA, high resistance to protease degradation and high permeability to the pulmonary mucus barrier. DRI-Pep #20 triggered cAMP elevation both *in vivo* in the airway tract of mice upon intratracheal administration, and *in vitro* in bronchial epithelial cells of cystic fibrosis (CF) patients. In CF cells, DRI-Pep #20 rescued the defective function of the cAMP-operated channel cystic fibrosis transmembrane conductance regulator, by boosting the efficacy of approved cystic fibrosis transmembrane conductance regulator modulators. Overall, this study unveils DRI-Pep #20 as a potent PI3K γ /PKA disruptor for achieving therapeutic cAMP elevation in chronic respiratory disorders.

The 3'-5'-cAMP second messenger controls different cellular processes, including cell growth and differentiation, gene transcription, and protein expression. cAMP exerts its function through the activation of different effectors, with protein kinase A (PKA) being the most widely characterized.

cAMP directly binds the dimer of the regulatory subunits of the PKA holoenzyme, promoting the release of the two catalytic counterparts, which are then free to phosphorylate various substrates. Although different G protein-coupled receptors (GPCRs) rely on the same second messenger cAMP for conveying signals within the cell, a tight spatial and temporal regulation of its concentration ensures that activation of a specific GPCR results in the appropriate cellular response (1). This local control of cAMP signals is achieved through multiprotein complexes that sequester enzymes responsible for cAMP generation (adenylyl cyclases) and destruction (phosphodiesterases, PDEs), as well as distinct signal transducers, in specific cellular locations. Key orchestrators of these "signaling islands" are A-kinase anchoring proteins (AKAPs) that, by definition, anchor PKA and its substrates and regulators to definite subcellular compartments (2). Perturbations of this fine control of cAMP compartmentalization underlie different pathologies, including cardiovascular and pulmonary diseases, cancer, neurological disorders, and inflammation. On these grounds, pharmacological manipulation of specific cAMP signalosomes with molecules blocking the interaction of AKAPs with either PKA or other components of the cAMP signaling pathway has been attempted and proven effective in preclinical models (2, 3).

Previous work identified the AKAP phosphoinositide 3-kinase γ (PI3K γ) as the core of a multiprotein complex which is central to smooth muscle contraction, immune cell activation, and epithelial fluid secretion in the airways (4). In the lungs, PI3K γ -bound PKA activates PDE4, ultimately restricting cAMP responses triggered by stimulation of β_2 -adrenergic receptors, the major GPCR mediating cAMP elevation in the airways. In agreement, inhibition of the PI3K γ /PKA interaction promotes local cAMP elevation, eventually resulting in airway smooth muscle relaxation and reduced neutrophil infiltration in a murine model of asthma. In

* For correspondence: Alessandra Ghigo, alessandra.ghigo@unito.it.

A nonnatural peptide targeting the AKAP function of PI3K γ

bronchial epithelial cells, targeting the PI3K γ AKAP function with a naturally occurring mimetic peptide (PI3K γ MP) enhances cAMP in the vicinity of the cystic fibrosis transmembrane conductance regulator (CFTR), the ion channel that regulates mucus hydration, thereby driving the opening of the WT channel, while synergizing with CFTR modulators in reinstating the function of F508del-CFTR, the most prevalent mutant in cystic fibrosis (CF) (4).

Here, we report the design of a nonnaturally occurring peptide, named D-retroinverso (DRI)-Pep #20, that acted as a potent disruptor of the PI3K γ /PKA complex by mimicking the core of the native interaction of PI3K γ with PKA, and that was characterized by nanomolar affinity for PKA, high resistance to protease degradation and high permeability to the pulmonary mucus barrier. Peptide-based inhibition of the PI3K γ /PKA interaction triggered cAMP elevation both *in vitro* in bronchial epithelial cells and *in vivo* in the airway tract of mice after intratracheal administration. Finally, the cAMP elevation elicited by DRI-Pep #20 rescued the defective function of the cAMP-operated channel CFTR in *in vitro* models of CF.

Results

DRI-Pep #20 is a PI3K γ /PKA disruptor with high binding affinity for PKA

DRI-Pep #20 was obtained by linking the nonnatural D-peptide RHQ GK to the DRI-isoform of the cell penetrating peptide Penetratin 1 (P1) by means of a glycine (G) linker (Fig. 1A). First, we determined the ability of DRI-Pep #20 to directly bind the PKA regulatory subunit RII α (PKA-RII α), the PKA isoform that we previously demonstrated being specifically bound by PI3K γ (5). To this end, we performed *in vitro* steady-state fluorescence spectroscopy using a recombinant fluorescein 5-maleimide-labeled PKA-RII α (PKA-F5M) (Fig. 1B), which retained the same activity as its unlabeled counterpart (Fig. S1, A and B). These experiments revealed that the peptide could associate recombinant PKA-RII α with high affinity, being the equilibrium dissociation constant (K_D) in the nanomolar range (76 nM; Fig. 1C). Further fast kinetic studies showed that DRI-Pep #20 rapidly associates to PKA-RII α forming a relatively stable complex. The association rate constant (K_{on}) in the order of $10^{-6} \text{ M}^{-1}\text{s}^{-1}$ indicated a quick assembly of the DRI-Pep #20/PKA-RII α complex, while the moderate dissociation rate (K_{off}) suggested a certain level of stability in the bound state (Fig. 1D and Table 1). Notably, DRI-Pep #20 associated to PKA as quickly as the naturally occurring PI3K γ MP peptide yet remained in the bound state for longer, with a K_{off} being 28-fold lower than that of the natural peptide (Fig. 1D and Table 1). In agreement with the high affinity of DRI-Pep #20 to PKA-RII α , the peptide inhibited the interaction between recombinant PI3K γ and F5M-labeled PKA-RII α up to 74%, and with an IC_{50} of 0.16 μM , while PI3K γ MP only displaced 50% of the PI3K γ /PKA-RII α complex with an IC_{50} of 1.5 μM (Fig. 1, E and F). Next, we tested whether DRI-Pep #20 could disturb the

anchoring of PKA by AKAPs other than PI3K γ . The ability of the peptide to raise cAMP levels in PI3K γ -deficient cells was used as a proxy of its capacity to interfere with other AKAP-based signalosomes (4). We found that DRI-Pep #20 failed to raise cAMP in cells that did not express its target PI3K γ , demonstrating that the peptide retained the selectivity for the PI3K γ -directed pool of PKA, despite the high binding affinity for PKA-RII α (Fig. 1G). Overall, these data identify DRI-Pep #20 as a potent and selective disruptor of the PI3K γ /PKA complex.

DRI-Pep #20 mimics the native interaction between PI3K γ and PKA-RII α

Next, we sought to elucidate the determinants of the high-affinity interaction of DRI-Pep #20 with PKA-RII α . Predictions of the tridimensional structure of DRI-Pep #20 suggested the presence of an α -helix, flanked by two uncoiled regions (Fig. 2A). The helical propensity of the peptide was confirmed by CD analyses showing a double-peak signal, with a maximum at 200 nm which is typical for α -helix structures, and a minimum in the 220 to 240 nm region which is characteristic for random-coil domains (6) (Fig. 2B). *In silico* simulations of the binding of DRI-Pep #20 to the docking/dimerization domain of PKA-RII α , the typical binding surface for AKAPs which spans amino acids 1 to 45 (2), revealed that all five amino acids of the RHQ GK sequence (R-1, H-2, Q-3, G-4, and K-5) could form intermolecular contacts with partners in the PKA-RII α dimer (Figs. 2C, S2A, and Table S1). Intriguingly, DRI-Pep #20 primarily interacted with amino acids 22 to 44 of the docking/dimerization domain (Fig. S2B), a region not bound by the classical AKAP disrupting peptide, Ht31 (7) (Fig. S3 and Table S1). Systematic amino acid substitutions within the RHQ GK sequence confirmed the importance of positively charged and polar amino acids in position three and four for the interaction of DRI-Pep #20 with PKA-RII α . Indeed, peptide variants bearing hydrophobic residues in those positions had reduced ability to disrupt the PI3K γ /PKA interaction, and thus to elevate cAMP in human bronchial epithelial cells (16HBE14o-), as compared to the parent sequence (Fig. S4A and Table S2). These observations suggested that a short amino acid sequence enriched in hydrophilic residues could form the backbone for the anchoring of PKA by PI3K γ and prompted us to better characterize the native interaction between the N-terminal domain of PI3K γ , which encompasses the putative PKA-binding motif (4, 5), and PKA-RII α . *In silico* simulations of the binding between PI3K γ and 2 to 44 PKA-RII α identified a region enriched in hydrophilic amino acids, spanning from K-126 to R-130 (KATHR), that could maximally interact with PKA (Figs. 3A and S5A). Intriguingly, the KATHR sequence phenocopied the complete PKA-binding motif of PI3K γ in raising cAMP in 16HBE14o-cells (Fig. S6A and Table S3), indicating that the core of the interaction between PI3K γ and PKA-RII α could reside within this region. In agreement, structural predictions and

A nonnatural peptide targeting the AKAP function of PI3K γ

Table 1
Binding kinetics of the interaction between DRI-Pep #20 or PI3K γ MP and PKA-RII α .

Binding constants	Steady-state experiment		Kinetic experiment	
	PI3K γ MP	DRI-Pep #20	PI3K γ MP	DRI-Pep #20
K_{ON} (10^6 M $^{-1}$ s $^{-1}$)	-	-	1.0	1.5
K_{OFF} (s $^{-1}$)	-	-	2.0	0.072
K_A (10^7 M $^{-1}$)	0.013	1.3	0.05	2.0
K_D (10^{-6} M)	7.5	0.076	2.0	0.049

K_A , association constant; K_D , dissociation constant; K_{on} , association rate constant; K_{off} , dissociation rate constant.

Taken together, these results demonstrate that the nonnatural peptide DRI-Pep #20 acts as a potent PI3K γ /PKA disruptor by mimicking the core of the native interaction of PI3K γ with PKA-RII α .

DRI-Pep #20 has favorable mucus permeability and protease resistance

Next, we sought to determine to what extent DRI-Pep #20 could be used for targeting the native PI3K γ /PKA complex in pulmonary cells to modulate cAMP for therapeutic purposes. In 16HBE140- cells, DRI-Pep #20 triggered a sustained elevation in cAMP levels (Fig. S8A), which declined 8 h poststimulation. In addition, the peptide demonstrated favorable tolerability, with an LD₅₀ that was 10-fold higher than the EC₅₀ (Fig. S8, B and C). *In vivo*, DRI-Pep #20 induced a dose-dependent increase in cAMP levels in both the trachea and lungs of intratracheally dosed mice (Fig. 4A), with EC₅₀ values of 8.06 μ g/Kg and 11.78 μ g/Kg, respectively (Fig. 4, B and C). Of note, cardiac cAMP concentrations were unchanged (Fig. 4D), suggesting that the peptide locally increased airway cAMP without systemic effects at the tested dose. In addition, a dose equivalent to the EC₅₀ did not further increase airway cAMP in mice lacking the PI3K γ protein, further corroborating the specificity of action of the compound (Fig. 4, E–G).

Since the efficacy of inhaled therapies can be hampered by extracellular barriers imposed by diseased lungs, including a thick layer of protease-rich mucus (8), we next sought to determine to what extent DRI-Pep #20 could penetrate mucus layers and resist to protease degradation. DRI-Pep #20 penetrated the phospholipid membrane in the parallel artificial membrane permeability assay (PAMPA) system (Fig. 5A) with an apparent permeability (P_{app}) of 1.88×10^{-6} cms $^{-1}$ (Fig. 5B). Of note, the addition of pathological CF sputum on top of the phospholipid layer (Fig. 5A) did not significantly affect the P_{app} of the peptide (P_{app} 2.55×10^{-6} cms $^{-1}$) (Fig. 5B), which remained within the range typical for medium-permeable compounds (9). To verify whether the favorable mucus permeability of DRI-Pep #20 could be ascribed to molecular dimensions compatible with the mesh size of CF mucus (10), transmission electron microscopy (TEM) and dynamic light scattering (DLS) assays were performed. TEM images showed that DRI-Pep #20 formed irregular aggregates of 5 to 40 nm in

size (Fig. 5C), in agreement with the particle diameter of 10 to 20 nm retrieved by DLS analysis (Fig. 5D).

Next, we tested whether DRI-Pep #20 retained the ability to elevate cAMP in pulmonary cells in the presence of neutrophil elastase, the most abundant protease in the lungs of patients with neutrophilic airway diseases, including but not limited to chronic obstructive pulmonary disease (COPD) and CF (11). The ability of the peptide to raise cAMP in 16HBE410- cells was completely unaltered by the presence of 3 μ g/ml of recombinant human neutrophil elastase (HNE) (Fig. 5E), a dose which was previously shown to inactivate other therapeutic peptides (12). Conversely, the cAMP elevating activity of the non-DRI isoform, Pep #20, was reduced by 26% by means of HNE (Fig. 5E). Notably, the activity of the DRI isoform was entirely preserved even in the presence of a 10-fold higher concentration of HNE (Fig. 5F), an amount that is typically detected in the lungs of patients with severe bronchiectasis (11), which was in line with the absence of any predicted cleavage sites by HNE (Fig. S9A). The observed resistance of DRI-Pep #20 to degradation was confirmed in the presence of a more complex biological matrix containing other proteases that could potentially cleave the peptide (Fig. S9B), that is CF sputum, where the DRI-Pep #20 retained 72% of its biological activity (Fig. 5G).

Taken together, these data demonstrate the ability of DRI-Pep #20 to elevate lung cell cAMP in the presence of a hostile extracellular environment composed of a mucus barrier enriched in proteases, which is typical of diseased lungs.

DRI-Pep #20 promotes cAMP-dependent activation of WT and F508del-CFTR in human bronchial epithelial cells

Next, we aimed to assess the extent to which DRI-Pep #20 could effectively restore cAMP levels and consequently reactivate the function of CFTR, a cAMP-dependent chloride channel impaired in a range of respiratory disease, including but not limited to COPD and CF (13). First, we assessed the ability of the peptide to stimulate the activity of the WT channel in 16HBE1410- cells expressing the halide-sensitive yellow fluorescent protein (HS-YFP) (Fig. 6B), which allows quantifying CFTR activity based on the fluorescence quenching rate elicited by an iodide influx (14). DRI-Pep #20 induced a 60% reduction in YFP fluorescence, which was completely prevented by coapplication of the CFTR inhibitor, CFTR_{inh-172} (Fig. 6B), demonstrating selective activation of CFTR channels. Of note, a control peptide containing only the cell penetrating moiety Penetratin 1 did not impact the fluorescence quenching rate. This further confirms that the effects observed with DRI-Pep #20 were not due to changes in membrane permeability but were instead associated with direct stimulation of CFTR activity (Fig. 6B). Dose-response experiments revealed an EC₅₀ of 20 μ M (Fig. 6C) and demonstrated that 25 μ M DRI-Pep #20 was as effective as 10 μ M forskolin, the adenylyl cyclase activator, in triggering CFTR gating in 16HBE1410- cells (Fig. 6D).

Further, we evaluated to what degree DRI-Pep #20 could reinstate the activity of F508del-CFTR in combination with the standard of care, including two CFTR correctors (elexacaftor/

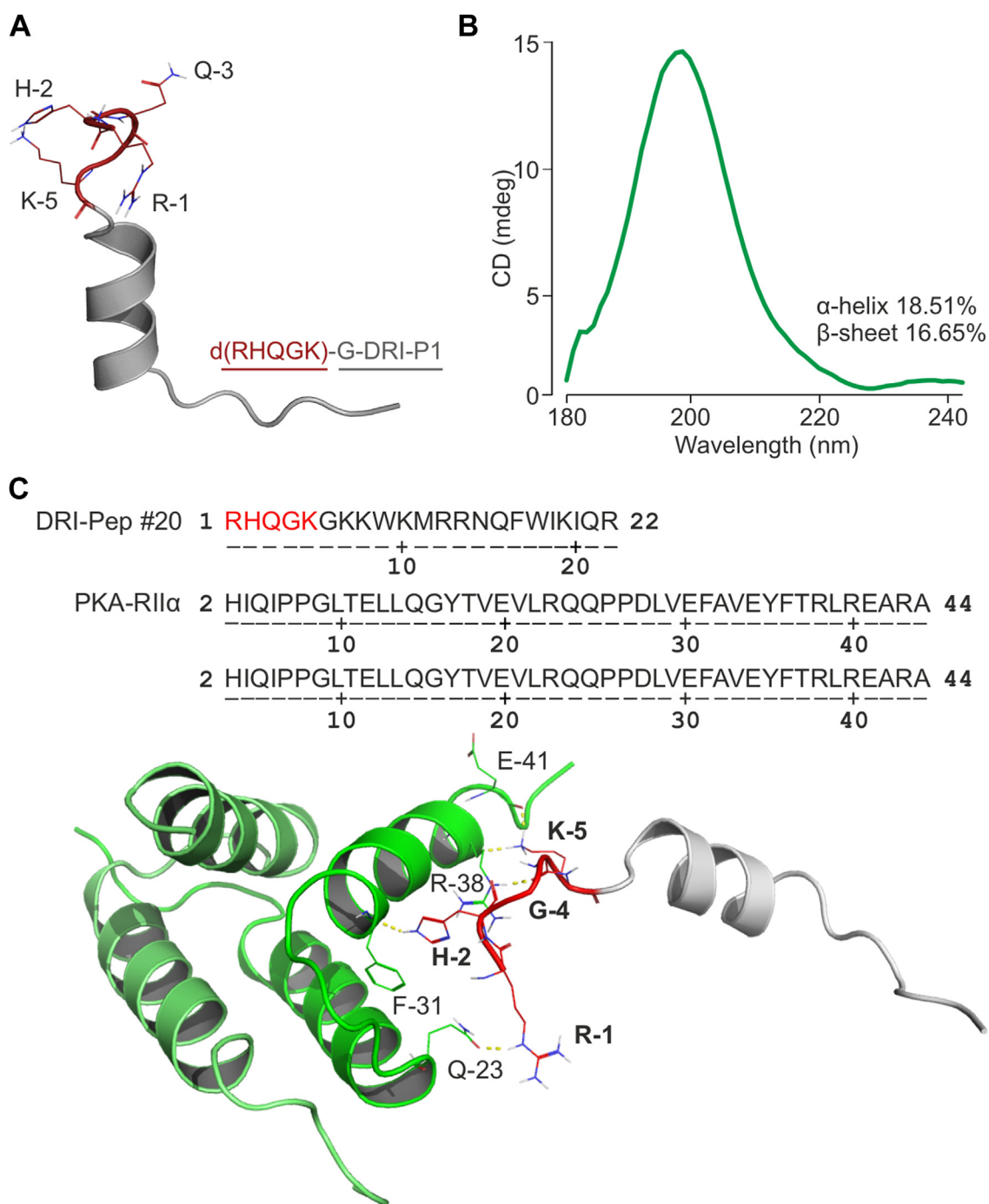


Figure 2. Structural prediction of the binding between DRI-Pep #20 and PKA-RII α . A, DRI-Pep #20 structure prediction by PEP-FOLD3.5. P1-G and RHQGK domains are shown as cartoons in gray and red, respectively. R-1, H-2, Q-3, and K-5 residues are indicated and shown as sticks. B, circular dichroism spectra of DRI-Pep #20 showing a peak at 190–240 nm. The percentage of α -helical and β -sheet secondary structures calculated by the K2D3 software are indicated. C, molecular docking simulation of the interaction between DRI-Pep #20 and the PKA-RII α dimer by HADDOCK 2.4. The docked pose of DRI-Pep #20 in complex with residues 2 to 44 of PKA-RII α (cartoon in green) is shown. The key residues involved in the binding are indicated and shown as sticks, with DRI-Pep #20 residues in bold. Hydrogen bonds between DRI-Pep #20 and PKA-RII α are indicated by yellow dashed lines. In (A and C), the structural models were developed using PyMOL. DRI, D-retroinverso; HADDOCK, high ambiguity driven biomolecular DOCKING; PI3K γ , phosphoinositide 3-kinase gamma; PKA, protein kinase A; PKA-RII α , PKA regulatory subunit RII α .

tezacaftor) and one CFTR potentiator (ivacaftor), that partially rescue the trafficking and gating defects of the mutant channel, respectively (15). In CF bronchial epithelial cells overexpressing the F508del-CFTR mutant and the HS-YFP, elxacaftor/tezacaftor/ivacaftor (ETI) produced a reduction of YFP

fluorescence of 50%, which was further decreased down to 25% when DRI-Pep #20 was added together with ETI (Fig. 6E).

Hence, these data support the use of DRI-Pep #20 as a single agent or as an add on to CFTR modulators, to therapeutically stimulate the activity of WT and F508del-CFTR, respectively.

A nonnatural peptide targeting the AKAP function of PI3K γ

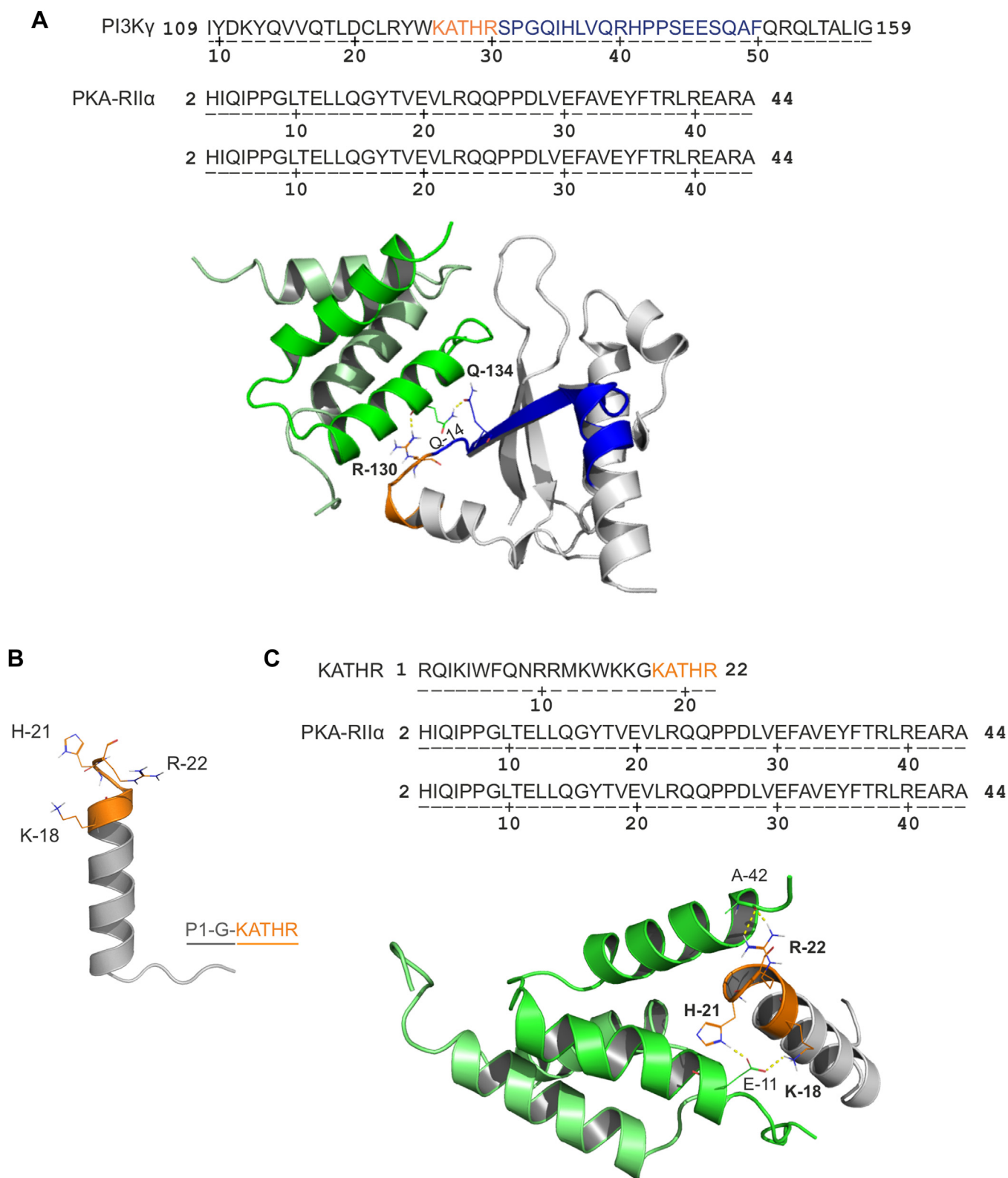


Figure 3. Structural prediction of the native binding between the N-terminal domain of PI3K γ and PKA-RII α . A, molecular docking simulation of the interaction between PI3K γ and the PKA-RII α dimer by HADDOCK 2.4. The docked pose of residues 109 to 159 of PI3K γ in complex with residues 2 to 44 of the PKA-RII α dimer (green cartoon) is shown. The amino acids critical for the binding between the two proteins are shown and indicated as sticks, with the residues of PI3K γ in *bold*. The putative PKA-binding motif of PI3K γ (126–150) is shown in orange and blue. The sequence in orange indicates the region of PI3K γ that was identified as being at the core of the interaction (KATHR). Hydrogen bonds between PI3K γ and PKA-RII α are indicated by yellow dashed lines. B, structural prediction of the KATHR sequence by PEP-FOLD3.5. KATHR and P1-G domains are shown as cartoons in orange and gray, respectively. K-18, H-21 and R-22 residues of the KATHR sequence (corresponding to K-126, H-129 and R-130 of native PI3K γ) are indicated and shown as sticks. C, molecular docking simulation of the interaction between KATHR and the PKA-RII α dimer by HADDOCK 2.4. The docked pose of KATHR in complex with residues 2 to 44 of the PKA-RII α dimer is shown. The amino acids critical for the binding between the two proteins are shown and indicated as sticks, with the residues of KATHR in *bold*. The putative PKA-binding motif of KATHR (1-22) is shown in orange and gray. The sequence in orange indicates the region of KATHR that was identified as being at the core of the interaction (KATHR). Hydrogen bonds between KATHR and PKA-RII α are indicated by yellow dashed lines.

A nonnatural peptide targeting the AKAP function of PI3K γ

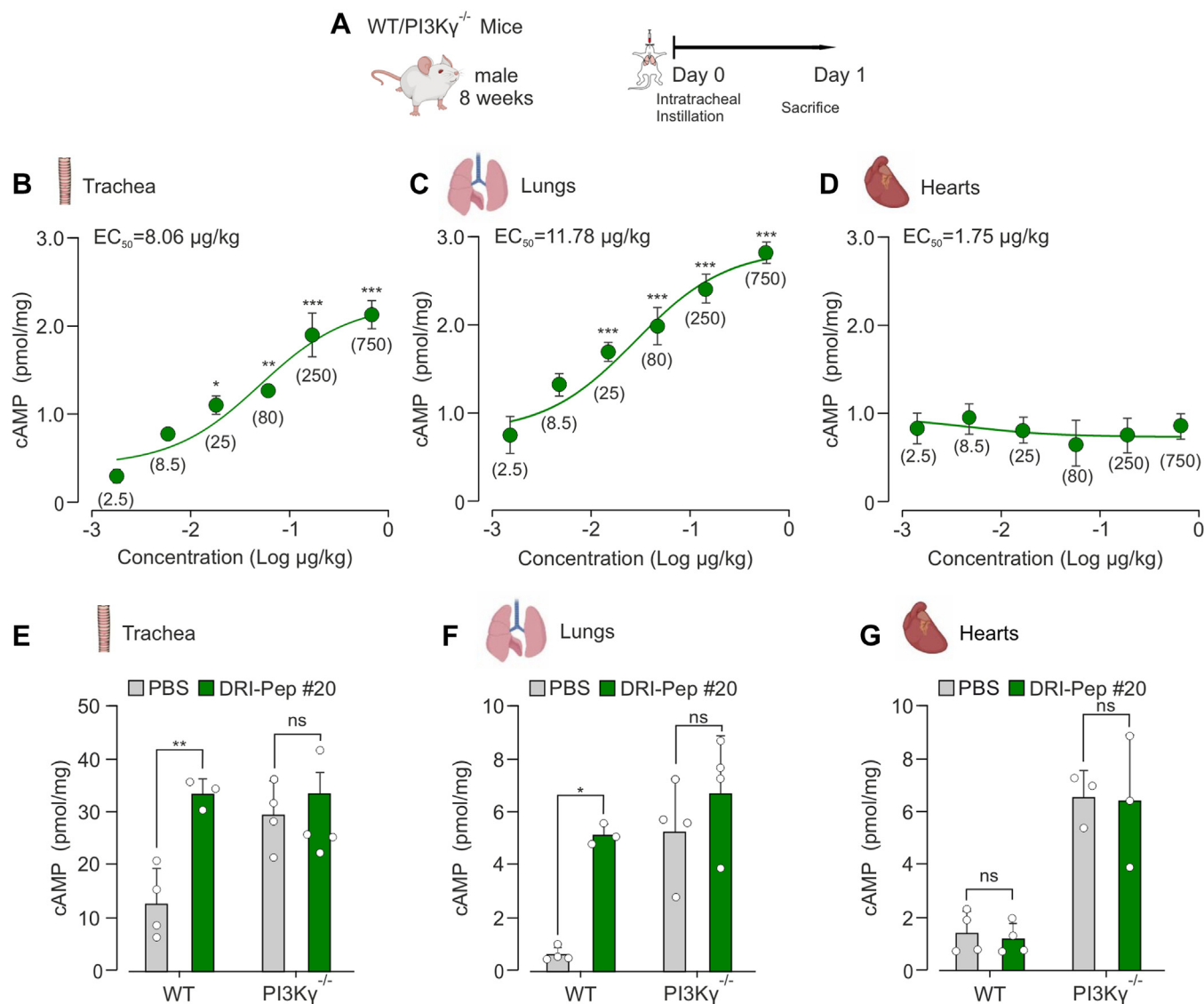


Figure 4. DRI-Pep #20 increases cAMP levels locally *in vivo* in the airway tract of mice. *A*, schematic representation of the treatment schedule. Mice received DRI-Pep #20 through intratracheal (i.t.) instillation. *B–D*, cAMP concentrations in tracheas (*B*), lungs (*C*) and hearts (*D*) from BALB/c mice 24 h after i.t. instillation of different doses of DRI-Pep #20 (0–750 mg/kg). Values in *brackets* indicate the dose of DRI-Pep #20 expressed as mg/kg. The number of mice (*n*) ranged from three to six per group. EC₅₀, median effective concentration. *E–G*, cAMP concentrations in tracheas (*E*), lungs (*F*) and hearts (*G*) from WT and PI3K $\gamma^{-/-}$ mice 24 h after i.t. instillation of 10 μ g/Kg DRI-Pep #20 (in *green*) or PBS (in *gray*). The number of mice (*n*) ranged from three to four per group. In (*A* and *B*), **p* < 0.05, ***p* < 0.01 and ****p* < 0.001 by one-way ANOVA, followed by Bonferroni's *post hoc* test. In (*E* and *F*) **p* < 0.05 and ***p* < 0.01 PBS versus DRI-Pep #20 by two-way ANOVA test, followed by Bonferroni's *post hoc* analysis. Throughout, data are means \pm SD. DRI, D-retroinverso; PI3K γ , phosphoinositide 3-kinase γ .

Discussion

Our study identifies a nonnatural peptide that functions as a selective and potent disruptor of the PI3K γ /PKA-RII α complex. This peptide, named DRI-Pep #20, serves as an effective tool to study PKA anchoring and manipulate cAMP/PKA signaling for therapeutic purposes.

Our structural predictions and molecular docking studies indicate that DRI-Pep #20 operates similarly to other AKAP disruptor peptides by mimicking the typical α -helical structure through which AKAPs bind PKA (16). In addition, our results

support previous research showing that, within this α -helix, the presence of polar and positively charged amino acids is crucial for the binding between the scaffold and the kinase (16). In contrast to other AKAP disruptors, DRI-Pep #20 uniquely interferes with the binding between PKA and PI3K γ , without affecting PKA pools anchored by other AKAPs. This specificity can be attributed to our earlier and current observations that the PKA-anchoring sequence of PI3K γ diverges from that of classical AKAPs (4, 5) and targets a different region of PKA compared to classical nonspecific AKAP

44 of PKA-RII α (cartoon in *green*) is shown. *Yellow dashed lines* indicate hydrogen bonds between KATHR and 2 to 44 PKA-RII α . The amino acids critical for the binding are indicated and shown as *sticks*, with KATHR residues in *bold*. Throughout, the structural models were developed using PyMOL. HADDOCK, high ambiguity driven biomolecular DOCKing; PI3K γ , phosphoinositide 3-kinase gamma; PKA, protein kinase A; PKA-RII α , PKA regulatory subunit RII α .

A nonnatural peptide targeting the AKAP function of PI3K γ

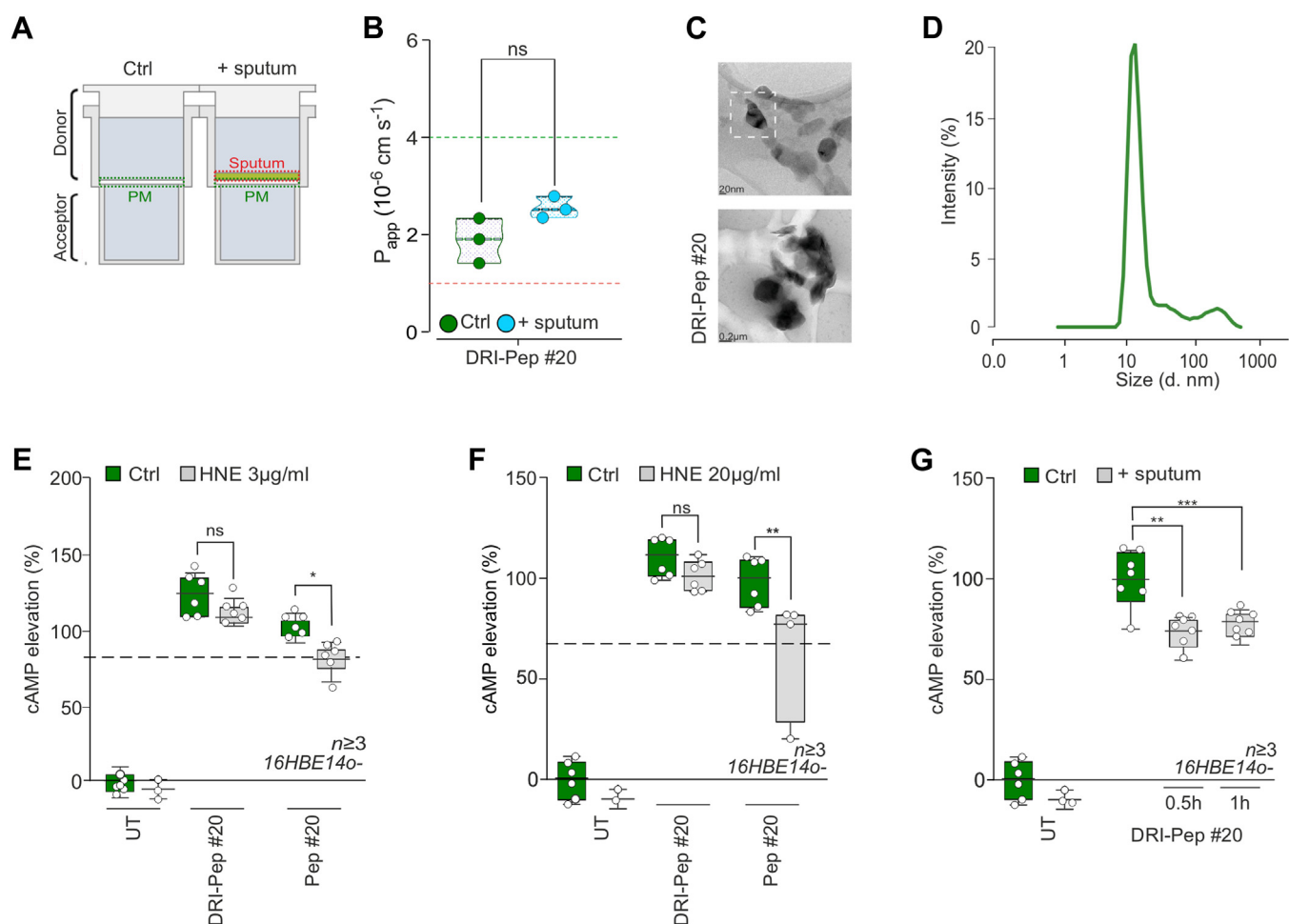


Figure 5. DRI-Pep #20 can penetrate pathological mucus and resist protease degradation. **A**, schematic representation of the parallel artificial membrane permeability assay (PAMPA) with and without cystic fibrosis (CF) sputum deposition on top of the artificial lipid membrane (PM). **B**, apparent permeability (P_{app}) measurements of DRI-Pep #20 (2 mg/ml) in the absence (green box) and in the presence (blue box) of CF sputum. The green dashed line indicates the P_{app} typical of high-medium permeable compounds ($4 \times 10^{-6} \text{ cm s}^{-1}$), while the red dashed line denotes the P_{app} of medium-low permeable molecules ($1 \times 10^{-6} \text{ cm s}^{-1}$). ns: nonsignificant by Student's *t* test. **C**, representative transmission electron microscopy (TEM) images of DRI-Pep #20 (0.1 mg/ml in water). The scale bar represents 20 nm. **D**, size distribution profile of DRI-Pep #20 (4 mg/ml in 2 mM PBS) obtained by dynamic light scattering (DLS) analysis. **E** and **F**, cAMP concentrations in 16HBE14o- cells treated with the DRI-Pep #20 and Pep #20 (25 μM for 30 min) in the absence (green bars) and in the presence (gray bars) of either 3 $\mu\text{g/ml}$ (**E**) or 20 $\mu\text{g/ml}$ (**F**) human neutrophil elastase (HNE). The amount of cAMP was expressed as percentage of cAMP accumulation elicited by Pep #20 without HNE. Dashed lines indicate the amount of cAMP (%) induced by Pep #20 with HNE as a reference. $n \geq 6$ technical replicates from $N > 3$ independent experiments. * $p < 0.05$ and ** $p < 0.01$ by one-way ANOVA, followed by Bonferroni's *post hoc* test. **G**, cAMP elevation in 16HBE14o- cells covered with a layer of CF sputum and then treated with 25 μM DRI-Pep #20 for 30 min and 1 h. The amount of cAMP was expressed as percentage of cAMP accumulation elicited by DRI-Pep #20 in the absence of sputum at 30 min ** $p < 0.01$ and *** $p < 0.001$ versus DRI-Pep #20 without sputum by two-way ANOVA test, followed by Bonferroni's *post hoc* analysis. $n \geq 6$ technical replicates from $N > 3$ independent experiments. Throughout, data are means \pm SD. DRI, D-retroinverso; ns, non-significant.

disruptor peptides, like Ht31. While our previous report pinpointed amino acids 126 to 150 as the PKA-anchoring sequence of PI3K γ (4, 5), the critical residues for the interaction remained elusive, partly due to the lack of the crystallographic structure of the PI3K γ N-terminal domain. In this study, our *in silico* characterization of the high-affinity interaction of DRI-Pep #20 with PKA-RII α sheds light on the native association between PI3K γ and PKA. Our computational modeling demonstrates that the KATHR sequence, encompassing amino acids 126 to 130 of the N terminal of PI3K γ , plays a central role in guiding the interaction with PKA. Like DRI-Pep #20, the KATHR peptide can adopt an α -helical conformation, establishing hydrogen bonds with partner amino acids within PKA-RII α , mainly through K-126, H-129, and R-130. Despite structural similarities, DRI-Pep #20

exhibits a significantly higher affinity for PKA compared to the native PKA-docking domain of PI3K γ , with a K_D value that is 100 folds lower than that obtained with the 126 to 150 region (5). This discrepancy raises questions about why nature selected a PI3K γ sequence with low affinity for PKA. It is plausible that, in physiological conditions, the binding between the two proteins needs to be sufficiently weak to allow PI3K γ to easily leave the complex, thereby interrupting PKA-mediated activation of PDEs, when necessary. This could serve as a protective mechanism against an excessive reduction of cellular cAMP below a critical level.

While the high binding affinity of DRI-Pep #20 to PKA-RII α can be attributed to the numerous hydrogen bonds that this nonnatural sequence can form with the kinase, its high proteolytic stability is a direct consequence of the presence of

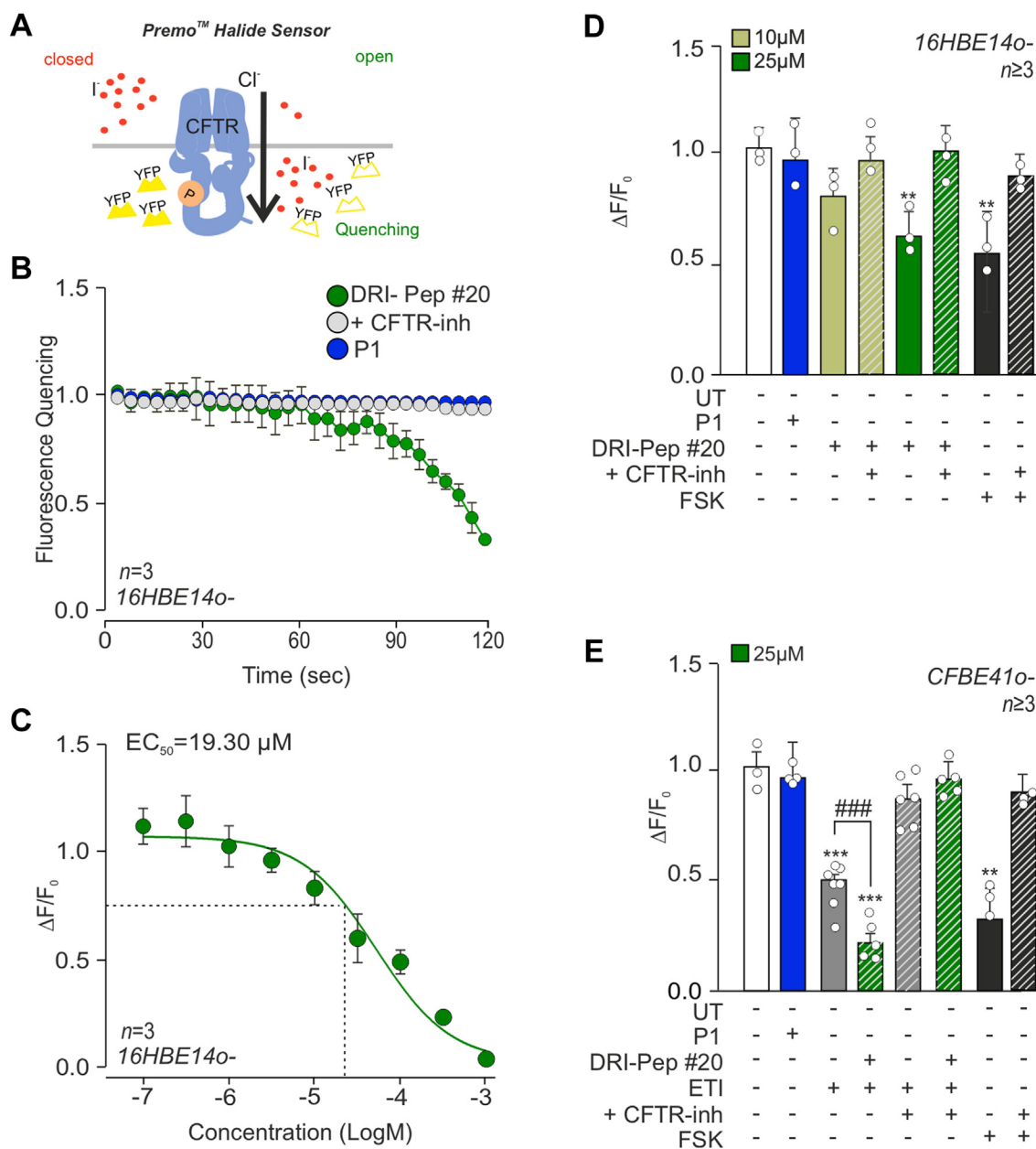


Figure 6. DRI-Pep #20 modulates WT and F508del-CFTR activity. *A*, schematic representation of CFTR activity measurement through the Premo Halide Sensor assay. *B*, average fluorescence quenching traces of 16HBE14o- cells expressing the halide-sensitive yellow fluorescent protein (HS-YFP) and treated with either 25 μM DRI-Pep #20 or equimolar amount of the control peptide P1 for 30 min before addition of Premo Halide stimulus buffer. Fluorescence was continuously read (1 point per second) starting at 1 s before addition of the buffer and up to 120 s. The CFTR inhibitor CFTR_{inh}-172 (10 μM for 5 min) was used to evaluate the selective activation of the CFTR channel. *C*, CFTR activity (expressed as the change in fluorescence $\Delta F/F_0$) in response to 30-min stimulation with increasing concentrations of DRI-Pep #20 (31.6 nM–316 mM) in 16HBE14o- cells expressing HS-YFP. To determine the EC_{50} , nonlinear regression analysis was used. *D*, CFTR activity (expressed as the change in fluorescence $\Delta F/F_0$) in 16HBE14o- cells expressing HS-YFP and treated with 10 to 25 μM DRI-Pep #20 for 30 min in the absence or in the presence of the CFTR inhibitor CFTR_{inh}-172 (10 μM for 5 min). The adenylyl cyclase activator, forskolin (FSK), was used as a positive control (100 nM for 5 min), while P1 was used as a negative control (25 μM for 30 min). *E*, CFTR activity in F508del-CFTR-CFBE41o- cells expressing HS-YFP and treated with elxacaftor/tezacaftor/ivacaftor alone (ETI) or together with DRI-Pep #20. Cells were corrected with elxacaftor (3 μM) and tezacaftor (10 μM) for 24 h and then exposed acutely to ivacaftor (1 μM) for 30 min, alone (ETI) or together with 25 μM DRI-Pep #20. The CFTR inhibitor CFTR_{inh}-172 was used as in (*B*). UT: untreated cells. In (*B* and *E*), $n \geq 3$ technical replicates from $N > 3$ independent experiments. $**p < 0.01$ and $***p < 0.001$ versus UT and $###p < 0.001$ ETI versus ETI plus DRI-Pep #20 by one-way ANOVA, followed by Bonferroni's *post hoc* test. Throughout, data are means \pm SD. CFBE, cystic fibrosis bronchial epithelial; CFTR, cystic fibrosis transmembrane conductance regulator; DRI, D-retroinverso; HS-YFP, halide-sensitive yellow fluorescent protein; P1, penetratin 1; UT, untreated cells.

D-amino acids, which are not recognized by proteases (17). The incorporation of nonnatural D-amino acids in a retro-reversed sequence, as in DRI-Pep #20, aims to obtain molecules with the same structure as the parent L-peptides, but with new chemical properties, such as increased half-life and

resistance to proteolytic degradation, which potentially improve their *in vivo* potency (18). These chemical features, and above all the high stability and target affinity, position DRI-Pep #20 as an ideal candidate for therapeutic cAMP modulation *in vivo*. Chronic respiratory diseases, where the

A nonnatural peptide targeting the AKAP function of PI3K γ

PI3K γ -PKA complex serves as a central signaling hub to multiple airway cell functions, like smooth muscle relaxation, epithelial ion transport and neutrophil infiltration (4), could significantly benefit from a treatment with DRI-Pep #20. Of note, DRI-Pep #20 remains confined in the lungs after local delivery, without reaching other tissues, like the heart, where cAMP elevation would be undesirable. Similar to what reported previously for the natural PI3K γ /PKA disruptor PI3K γ MP (4), the lack of systemic effects of DRI-Pep #20 may be attributable to its relatively large size. As a peptide of 3 kDa, DRI-Pep #20 may have limited ability to diffuse beyond the respiratory tract when administered locally at pharmacologically relevant doses, resulting in its confinement to the lungs. In addition to the local action, another added value of DRI-Pep #20 is its high stability in the presence of human neutrophil elastase, which supports the potential use of this peptide for achieving therapeutically relevant cAMP elevation in highly inflamed lungs. This is of particular relevance in a range of airway diseases, including COPD, certain forms of asthma, non-CF bronchiectasis (NCFB), and even in patients with CF who may still experience airway inflammation despite highly effective modulator therapies targeting the basic genetic defect of the disease (19, 20).

In addition to proteases associated with inflammation, another challenge posed by diseased lungs is the thick mucus layer covering respiratory epithelia (8). Especially in patients with CF and NCFB, mucus may reduce the bioavailability of inhaled therapeutics decreasing their overall efficacy. Although a layer of sputum over epithelial cells may not fully replicate the thick, dense mucus plugs observed *in vivo*—highlighting the need for further research—our assays using patient-derived sputum as a model for CF mucus indicated that DRI-Pep #20 is not significantly impacted by the barrier properties of the mucus. Moreover, in spite of being a relatively large molecule (MW \sim 3 kDa), DRI-Pep #20 is well below the mesh size of the pathological mucus. TEM and DLS analyses indicate that the peptide can form aggregates of 20 nm in size, which could freely diffuse through the 100 to 1000 nm meshes of the network of bundled fibers that are typically formed by biopolymers in the CF mucus and that are filled with a low viscosity fluid (21).

These observations imply that, in diseased lungs, relevant doses of DRI-Pep #20 could reach the underlying epithelial cells wherein targeting the PI3K γ /PKA complex is anticipated to boost CFTR activity (4). Our data indicates that in CF bronchial epithelial cells DRI-Pep #20 enhances the effects of the standard combination of CFTR modulators, ETI, in rescuing the activity of the most common CFTR mutant, F508del. These findings carry significant clinical implications, especially in light of recent studies demonstrating that CFTR potentiators and correctors only partially restore the function of mutant channels, achieving up to 60% the WT CFTR levels (22–24). Consequently, CF patients treated with highly effective modulator therapy may still experience residual mucus dysfunction, airway infection, and inflammation (19, 20, 25) and could significantly benefit from the ability of DRI-Pep #20 to maximize the clinical efficacy of the standard-of-care. In

addition, our observation that the peptide itself activates the WT form of the CFTR channel supports the prospect of extending the use of DRI-Pep #20 to treat a range of nongenetic conditions characterized by acquired CFTR dysfunction, including COPD, nonatopic asthma, and NCFB (13).

In summary, our study identified a nonnatural peptide that specifically targets the AKAP function of PI3K γ , demonstrating unprecedented binding affinity and potency. With its resistance to proteases and ability to penetrate airway mucus, DRI-Pep #20 shows potential for elevating therapeutic cAMP levels in chronic respiratory disorders where mucus accumulation and inflammatory remodeling remain significant unmet medical needs. Although DRI peptides have demonstrated tolerability and therapeutic efficacy in clinical trials (26), further preclinical testing in both rodents and non-rodents is required to assess the feasibility of developing an inhaled therapy based on DRI-Pep #20 for human use.

Experimental procedures

Peptides and reagents

Peptides were synthesized by GenScript at >95% purity. The sequences of all peptides are listed in Tables S2 and S3.

Recombinant human PKA regulatory subunit RII α (PKA-RII α ; product code: PK-PKA-R2A025) and catalytic subunit C α (PKA-C α ; product code: PK-PKA-HCA050) were purchased from Biaffin GmbH & Co KG. PI3K γ catalytic subunit (p110 γ) was from Origene Technologies (TP307790).

Human neutrophil elastase was purchased from Sigma-Aldrich (CAS 9004-06-2, Sigma-Aldrich) and reconstituted in 50 mM sodium acetate, pH 5.5, with 200 mM NaCl. VX-809 (lumacaftor), VX-770 (ivacaftor), VX-661 (tezacaftor) and VX-445 (elexacaftor) were purchased from MedChemExpress LLC. Forskolin and CFTR_{inh}-172 were purchased from Sigma-Aldrich (CAS 66575-29-9).

Cell lines

Immortalized normal 16HBE14o- cells were kindly provided by Dr Gruenert (University of California San Francisco). Cystic fibrosis bronchial epithelial (CFBE41o-) cells stably expressing F508del-CFTR (F508del-CFTR-CFBE41o-) were kindly provided by L. Fu from the UAB Research Foundation (Birmingham, AL). Cells were grown in minimum essential medium supplemented with 10% fetal bovine serum, 5 mM L-Glutamine, 100 U/ml penicillin and 100 μ g/ml streptomycin (Thermo Fisher Scientific) on culture dishes precoated with human fibronectin (1 mg/ml; Sigma-Aldrich), bovine collagen I (3 mg/ml; Sigma-Aldrich) and bovine serum albumin (0.1%; Sigma-Aldrich) diluted in LHC-8 basal medium (Invitrogen). Cells up to passage 15 were used for experiments and tested negative for *mycoplasma* contamination prior to experimentation. All cells were cultured at 37 °C and under a 5% CO₂ atmosphere.

Animals

PI3K γ -deficient mice (PI3K γ ^{-/-}) were described previously (4). Mutant mice were back-crossed with C57Bl/6j mice for 15 generations to inbreed the genetic background, and C57Bl/6j

were used as controls (WT). Mice used in all experiments were 8 to 12 weeks of age. Mice were group-housed, provided free-access to standard chow and water in a controlled facility providing a 12-h light/dark cycle and were used according to institutional animal welfare guidelines and legislation, approved by the local Animal Ethics Committee. All animal experiments were approved by the animal ethical committee of the University of Torino and by the Italian Ministry of Health (Authorization n°757/2016-PR).

Isolation of murine peritoneal macrophages

Peritoneal macrophages were prepared from 8- to 12-week-old WT and PI3K $\gamma^{-/-}$ mice, as described previously (4). Briefly, cells were collected from euthanized animals by peritoneal lavage with 5 ml of PBS, supplemented with 5 mM EDTA. Cells were centrifuged for 3 min at 300 g, and the pellet was resuspended in culture media including RPMI media, 100 U/ml penicillin, and 100 μ g/ml streptomycin, and 10% heat-inactivated fetal bovine serum (Thermo Fisher Scientific). Macrophages were seeded in 96-well plates (1×10^6 cells/well) and maintained at 37 °C with 5% CO₂ for at least 16/18 h before treatment with the peptide and cAMP quantification.

cAMP measurements

From cells

cAMP content was measured in 16HBE14o- cells at the indicated time points after treatment with the indicated doses of peptides using the Promega cAMP-Glo Assay kit (Promega), according to the manufacturer's protocol.

From tissues

Lungs, tracheas, and hearts were collected from euthanized mice 24 h after intratracheal instillation of different doses of the peptide (0–750 mg/kg in a final volume of 50 μ l of PBS). Snap-frozen tissues were powdered in liquid nitrogen and extracted with cold 6% trichloroacetic acid. Samples were sonicated for 10 s, incubated at 4 °C under gentle agitation for 10 min and then centrifuged at 13,000 rpm at 4 °C for 10 min. Supernatants were washed four times with five volumes of water saturated with diethyl ether and lyophilized. cAMP content was detected with Cyclic AMP ELISA Kit (Cayman Chemical), according to the manufacturer's protocol.

Cell viability assay

Human bronchial epithelial cells (16HBE14o-) were seeded in 96-well plates (2×10^4 cells/well) and incubated for at least 16/18 h at 37 °C with 5% CO₂ before experiments. Non-adherent cells were eliminated by washing with PBS and cells were then stimulated with eight different doses of the indicated peptide (0 μ M–1 mM range) for 24 h. ATP levels were evaluated as an indicator of viable cells using the CellTiter-Glo Luminescent Cell Viability Assay (Promega), according to the manufacturer's protocol. The lethal dose (LD₅₀) was calculated with respect to untreated control cells, whose viability was set to 100%.

CFTR activity measurements

CFTR-mediated anion transport was measured by using the Premo Halide Sensor (Thermo Fisher Scientific) which allows assessment of CFTR activity by measuring the rate of YFP fluorescence quenching caused by iodide/chloride exchange across the plasma membrane. Briefly, the HS-YFP was expressed in 16HBE14o- and F508del-CFTR-CFBE41o- cells through the BacMam technology, according to the manufacturer's protocol. Cells expressing the HS-YFP were cultured on 96-well plates and treated with the indicated peptides/compounds for the indicated time. Fluorescence was evaluated in a plate reader immediately after addition of 150 μ l of Halide stimulus buffer (an NaI-containing solution) leading to a final NaI concentration in the wells of 75 mM. Fluorescence was continuously read (1 point per second) starting at 1 s before Halide stimulus buffer addition and up to 120 s. CFTR activity was expressed as $\Delta F/F_0$ where ΔF was obtained by subtracting the background fluorescence (fluorescence of cells not expressing HS-YFP) to the fluorescence measured at the specific time point after addition of NaI. ΔF was then normalized to the initial fluorescence F_0 (fluorescence of HS-YFP-expressing cells immediately after addition of NaI) to obtain a measure of relative fluorescence $\Delta F/F_0$.

CF sputum samples

Spontaneous expectorated sputum samples from CF patients in stable clinical conditions were collected at the Bronchiectasis and Cystic Fibrosis Programs of the Respiratory Department of Fondazione IRCCS Ca' Granda Ospedale Maggiore Policlinico in Milan (Italy) and processed as previously described (27). The study protocol was approved by local institutional review boards (594_2016bis) and all participants provided written informed consent to the collection and use of their biological samples. Briefly, samples were first processed by eliminating saliva, and then sputum plugs were selected and weighted. Samples were diluted 8 \times in PBS, vortexed until sputum dissolution and centrifuged for 15 min at 3000g. Supernatants were recovered and stored at –80 °C, thawed overnight at 4 °C, and all subsequent experiments were undertaken within 24 h from thawing. Neutrophil elastase was quantified as described previously (27) and sputum samples containing 20 μ g/ml of active neutrophil elastase were used to assess the activity of peptides in 16HBE14o- cells in the presence of CF sputum. Briefly, cells were seeded in 96-well plates (2×10^4 cells/well) and incubated for at least 16/18 h at 37 °C with 5% CO₂ before experiments. Subsequently, peptides were diluted in PBS at a final concentration of 25 μ M and a PBS: sputum mixture (1:1) was added on the top of adherent cells (100 μ l/well). cAMP levels were quantified at the indicated time points using the Promega cAMP-Glo Assay kit (Promega), according to the manufacturer's protocol.

Parallel artificial membrane permeability assay

To assess the permeability of peptides through a CF sputum layer, a PAMPA (Corning Gentest Pre-coated PAMPA, 353015, USA plates) that allows to measure the

A nonnatural peptide targeting the AKAP function of PI3K γ

ability of drugs to diffuse from a donor compartment, through an artificial membrane, into an acceptor compartment, was used as described previously (9). The bottom wells of the PAMPA system (“acceptor” wells) were filled with 300 μ l of PBS (10 mM, 150 mM NaCl, pH 7.4), while “donor” wells were filled with 200 μ l of the peptide solution (2 mg/ml in 10 mM PBS, 150 mM NaCl, pH 7.4), in the absence or presence of CF sputum. In the latter case, 40 μ l of CF sputum was first deposited over the PAMPA membrane, and the peptide solution was subsequently added over the CF sputum layer. Afterward, the two wells were coupled and incubated for 5 h at room temperature (RT). At the end of the incubation, the plates were split, and the amount of peptide diffused into the acceptor well was quantified by fluorescence spectroscopy using a Horiba Jobin Yvon Fluorolog 3 TCSPC fluorimeter (Horiba) equipped with a 450-W xenon lamp and a R928 photomultiplier (Hamamatsu Photonics). Excitation was performed at 280 nm while emission was recorded in the spectral region of 290 to 500 nm (maximum of emission at 362 nm). Excitation and emission slits were set at 4 and 5 nm, respectively. The concentration of the peptide was calculated using a 66-points calibration curve. The apparent permeability coefficient (P_{app}) was expressed according to this relationship:

$$P_{app} = \frac{dQ/dt}{C_0 \times A} \quad (1)$$

derived from Fick's law for steady-state conditions (28), where dQ is the quantity of drug expressed as moles permeated into the acceptor compartment at time t (18,000 s), C_0 is the initial concentration of the peptide in the donor well, and A is the area of the well membrane (0.3 cm²).

PKA-RII α bioconjugation and fluorescence spectroscopy

Recombinant PKA-RII α was bioconjugated to fluorescein 5-maleimide (F5M), as described previously (29), using 75 μ g of PKA-RII α and a 50-fold excess of F5M. After bioconjugation, the derivative was immediately purified using a Sephadex G-25 desalting column and PBS (20 mM, 150 mM NaCl, pH 7.2) as eluent. To evaluate F5M labeling efficiency, the dye/protein ratio (D/P) of the conjugates was determined by the absorption spectra of the labeled proteins in PBS (20 mM, 150 mM NaCl, pH 7.2), according to the following equation:

$$\frac{D}{P} = \frac{A_{max} e_{prot}}{(A_{280} - cA_{max}) e_{dye}} \quad (2)$$

where A_{280} is the absorption of the conjugate at 280 nm; A_{max} is the absorption of the conjugate at the absorption maximum of the corresponding F5M; c is a correction factor ($c = 0.29$); e_{prot} (25169 M⁻¹cm⁻¹) and e_{dye} (63096 M⁻¹cm⁻¹) are the molar extinction coefficients of PKA and F5M, respectively. PKA-RII α presents six cysteine residues, and the final D/P value was 0.2.

UV-visible absorption spectra were measured with a UH5300 spectrophotometer (Hitachi) at RT, using 1 cm pathway length quartz cuvette. Fluorescence emission spectra in steady-state mode were acquired at RT using a Jobin Yvon Fluorolog 3 TCSPC fluorimeter (Horiba) equipped with a 450-W Xenon lamp and a R928 photomultiplier (Hamamatsu Photonics). Steady-state fluorescence spectra were recorded in the 500 to 600 nm range. The excitation wavelength was set on 490 nm and the excitation and emission slits were set on 2 and 4, respectively. Equilibrium binding constants (K_D and K_A) were obtained from steady-state data.

Fluorescence kinetics were measured using an Applied Photophysics SX20 stopped-flow spectrophotometer (Applied Photophysics) fitted with a 495 nm cutoff filter between the cell and the fluorescence detector, and equipped with a thermostat bath set at 25 \pm 0.2 $^{\circ}$ C. Association and dissociation rate constants (k_{on} and k_{off}) were calculated from stopped-flow kinetics data. Data acquisition, visualization, and analysis were performed with Pro-Data software (<https://www.photophysics.com/service-support/documents-and-software/>) from Applied Photophysics Ltd (Applied Photophysics).

To assess the ability of DRI-Pep #20 and PI3K γ MP to displace the binding between PI3K γ and PKA-F5M, steady-state emission spectra of the PI3K γ /PKA-F5M complex in the presence of increasing concentrations of the peptide were acquired. Briefly, 50 nM of recombinant PI3K γ was added to 100 nM F5M-bounded PKA-RII α in a total volume of 100 μ l PBS. The concentration of the PI3K γ /PKA-F5M complex was kept constant while gradually titrated with increasing concentrations of the peptides. The complex was excited at 490 nm and emission spectra were recorded in the 500 to 600 nm spectral range, as described above. The degree of displacement of the PKA-RII α -PI3K γ complex was expressed as the percentage of fluorescence quenching after addition of the peptide.

In vitro interaction assay

Binding assays of either PKA-RII α or PKA-RII α -F5M (50 nM) with PKA-C α (50 nM) were performed in binding buffer (50 mM Tris-HCl pH 7.4, 20 mM NaCl, and 0.05% Triton X-100). Recombinant proteins were incubated for 30 min at RT under mild shaking, in the absence or the presence of 1.5 μ M cAMP. Afterward, 1 μ g of an antibody against PKA-RII α (Santa Cruz Biotechnology; product code: sc-137220) was added to the buffer and incubated for additional 30 min at 4 $^{\circ}$ C. Subsequently, 15 μ l of Fast Flow Protein G Sepharose beads (Millipore), previously washed and resuspended with PBS in a 2:1 ratio, were added to the reactions and incubated for 10 min at 4 $^{\circ}$ C under mild shaking. Finally, the beads were washed four times with binding buffer, and the proteins bound to the beads were eluted by treating them for 5 min at 95 $^{\circ}$ C in 2 \times Laemmli sample buffer. The eluted proteins were then subjected to SDS-PAGE.

PKA activity

PKA activity was measured by using the ADP-Glo Kinase Assay (Promega), which allows assessment of kinase activity by

measuring the amount of ADP produced during the kinase reaction. Briefly, PKA-RII α or PKA-RII α -F5M (100 nM) was incubated for 30 min at RT under mild shaking with 100 nM PKA-C α , in the absence or in the presence of 5 μ M ATP and 1.5 μ M cAMP. Subsequently, the assay was performed according to the manufacturer's protocol.

Circular dichroism

CD measurements were performed on a Jasco-810 Dichrograph equipped with a Peltier thermoelectric controller (Jasco Inc). The spectra of peptides were recorded in the continuous mode between 260 and 180 nm at 25 °C in 0.1 cm path length quartz cuvette (Hellma GmbH) with a total peptide concentration of 0.2 mg/ml dissolved in 2 mM PBS (0.6 mM KH₂PO₄ and 1.6 mM K₂HPO₄), pH 7.4. The CD spectrum in the 190 to 240 nm range was used to predict the secondary structural content of the peptide using the K2D3 web server (30).

Transmission electron microscopy and dynamic light scattering

Self-assembled peptide nanostructures were analyzed by TEM analysis. Transmission electron micrographs were obtained with a JEOL 3010-UHR TEM operating at an accelerating voltage of 300.00 kV (JEOL). TEM samples were prepared by dissolving the peptides at 0.1 mg/ml in water and drying them on a carbon-coated copper grid. The nominal magnification used to record nanostructures were 500,000 \times and 800,000 \times .

The size distribution profile of the self-assembled peptide was determined by DLS (Malvern Zetasizer). Samples were prepared at 4 mg/ml in 2 mM PBS (0.6 mM KH₂PO₄ and 1.6 mM K₂HPO₄), pH 7.4. Measurements were performed after an equilibration time of 60 s which allowed samples to reach the temperature of 25 °C.

Peptide mutagenesis

Systematic amino acid substitutions were performed using an in-house Python script. To identify which variant could mimic the characteristics of DRI-Pep #20, we compared the ability of each peptide to adopt the same spatial arrangement and exhibit a similar surface charge distribution. The peptides from the library were subsequently processed using Omega2 (OMEGA, version 4.1.0.2, <https://www.eyesopen.com/omega>; OpenEye Scientific Software: Santa Fe, NM) (31, 32), a software that creates a multiconformer structure database capable of reproducing biologically active conformations. The ROCS software (ROCS, version 3.4.1.2, <https://www.eyesopen.com/rocs>; OpenEye Scientific Software: Santa Fe, NM) (33) was employed to conduct a shape-based overlay method, in which molecules were aligned through a solid-body optimization process aimed at maximizing the volume overlap between them. Subsequently, the peptides were reranked for similarity to DRI-Pep #20 based on electrostatic properties using the EON program (EON, version 2.3.4.2, <https://www.eyesopen.com/eon>; OpenEye Scientific Software: Santa Fe, NM) (34). The final score assigned to

each peptide was based on a dual Tanimoto score, ranging from 0 to 2, where a score of two signifies an exact match in both shape and electrostatics between the two molecules. Peptides with the highest scores were considered for further analysis.

Protein structure prediction

The 3D structure of PI3K γ was downloaded by AlphaFold (<https://alphafold.ebi.ac.uk/>) (35) and validated by RMSD alignment of all the atoms with the cryo-electron microscopy structure of the heterodimeric PI3K γ complex, p110 γ -p101 (Protein Data Bank [PDB] ID 7MEZ) (36).

Peptide structure prediction

The structure of the peptides was predicted with PEP-FOLD3.5 (<https://bioserv.rpbs.univ-paris-diderot.fr/services/PEP-FOLD3/>) (37), a *de novo* approach that predicts peptide structures from amino acid sequences. Briefly, starting from the amino acid sequence, first a series of 200 simulations was run, each one sampling a different region of the conformational space using the Generator taboo-sampling 5 (ts5), recommended for peptides longer than 10 amino acids. The output was an archive of clusters of all the models sorted out using the template modeling score followed by performing the model quality assessment using Apollo (38). The first five models, representing the five best conformation of each cluster with the best scores defined according to the lowest sOPEP energy and the highest template modeling-score value, were selected and further supported by RMSD. The RMSD of each model was compared to the RMSD of residues 126 to 150 of the p110 γ structure, both the protein structure predicted by AlphaFold and the crystal structure (PDB ID 7mez, RCSB database) (36). Finally, the best structure of the peptide was validated by visual analysis on PyMOL (<https://pymol.org/>).

Docking studies

Docking studies were performed with the High Ambiguity Driven Biomolecular DOCKing (HADDOCK) software (<https://rascar.science.uu.nl/haddock2.4/>). Briefly, starting from the NMR dimeric structure of PKA-RII α (PDB ID 2KYG) (39), the 3D structure of PI3K γ and peptide structures, the HADDOCK docking ran three consecutive steps, first the molecules were randomly oriented, and a rigid-body search was performed (it0). The output was an archive of 1000 models, among them the top 200 ranked structures were selected based on the energy function and addressed to the semi-flexible simulated annealing stage performed in torsion angle space (it1). In the third stage, the structures were refined in Cartesian space with explicit solvent layer (water) and subjected to a short molecular dynamic simulation at 300 K. During the refinement, both the side chain and backbone of interface residues were progressively allowed to move.

The final models were automatically clustered based on the positional interface ligand RMSD (iL-RMSD) by fitting the conformational changes on the interface of the receptor (PKA-

A nonnatural peptide targeting the AKAP function of PI3K γ

RII α) and on the interface of the partners (p110 γ and the peptides). Finally, the binding poses were assessed by the HADDOCK report and the binding affinity was evaluated by protein binding energy prediction (PRODIGY) webserver (40, 41). The resulting best binding pose was validated by visual analysis on PyMOL.

Statistical analysis

Data are presented as scatter plots with bars (means \pm SD). Prism software (GraphPad Software Inc; <https://www.graphpad.com/>) was used for statistical analysis. Raw data were first analyzed to confirm their normal distribution *via* the Shapiro-Wilk test and then analyzed by unpaired Student's *t* test, one-way analysis of variance (ANOVA), or two-way ANOVA. Bonferroni correction (one-way and two-way ANOVA) was applied to correct for multiple comparisons. $p < 0.05$ was considered significant.

Data availability

All data associated with this study are available in the article or the [Supplementary Information](#).

Supporting information—This article contains supporting information (5).

Acknowledgments—Not applicable.

Author contributions—A. D. S., L. T., C. B., V. S., G. P., A. Murabito, O. V. G., E. M., L. T., F. B., A. G., S. A., A. M., S. V., E. H., and A. G. writing—review and editing; A. D. S., L. Tasca, C. B., and G. P. formal analysis; A. D. S., A. M., and S. V. methodology; A. D. S., L. Tasca, C. B., A. Murabito, O. V. G., A. M., investigation; A. D. S., V. S., A. Murabito, E. M., F. B., A. Gramegna, S. A., A. Murabito, E. M., E. H., and A. G. visualization; A. D. S. and A. G. conceptualization; A. D. S. and A. G. writing—original draft; A. D. S. validation; A. D. S., V. S., G. P., E. M., L. T., F. B., A. G., S. A., S. V., and E. H. data curation; L. T. resources; E. H. and A. G. supervision.

Funding and additional information—This work was supported by research grants from Cariplo Foundation (#2018-0498 to E. H.), Roche Foundation (Bando Roche per la Ricerca 2019 to A. G.), Compagnia di San Paolo (CSTO161109 to E. H.), Telethon Foundation (GGP20079 to A. G.), Research Grant Ministero della Salute, Italy (RC 2023/260-01 to F. B.), Fondazione IRCCS Ca' Granda Ospedale Maggiore Policlinico Milano, Regione Lombardia Cystic Fibrosis Funding 2022 (Cod. 18563 Capitolo 13.01.1 to F. B.) and PRIN 2022 (2022WHSC3 to S. A., F. B. and E. H.).

Conflict of interest—Alessandra Ghigo and Emilio Hirsch are co-founders and shareholders of Kither Biotech Srl. Valentina Sala and Laura Tasca are employees of Kither Biotech Srl. All other authors report no conflicts of interest with the contents of the article.

Abbreviations—The abbreviations used are: AKAPs, A-kinase anchoring proteins; CF, cystic fibrosis; CFBE, cystic fibrosis bronchial epithelial; CFTR, cystic fibrosis transmembrane conductance regulator; COPD, chronic obstructive pulmonary disease; DLS, dynamic light scattering; DRI, D-retroinverso; ETI, elexacaftor/tezacaftor/ivacaftor; GPCR, G protein-coupled receptor;

HADDOCK, high ambiguity driven biomolecular DOCKing; HNE, human neutrophil elastase; HS-YFP, halide-sensitive yellow fluorescent protein; NCFB, non-CF bronchiectasis; PAMPA, parallel artificial membrane permeability assay; PDB, Protein Data Bank; PDE, phosphodiesterase; PI3K γ , phosphoinositide 3-kinase gamma; PKA, protein kinase A; PKA-F5M, 5-maleimide-labeled PKA-RII α ; PKA-RII α , PKA regulatory subunit RII α ; RT, room temperature; TEM, transmission electron microscopy.

References

1. Zaccolo, M., Zerio, A., and Lobo, M. J. (2021) Subcellular organization of the cAMP signaling pathway. *Pharmacol. Rev.* **73**, 278–309
2. Omar, M. H., and Scott, J. D. (2020) AKAP signaling islands: venues for precision pharmacology. *Trends Pharmacol. Sci.* **41**, 933–946
3. Murabito, A., Cnudde, S., Hirsch, E., and Ghigo, A. (2020) Potential therapeutic applications of AKAP disrupting peptides. *Clin. Sci. (Lond)* **134**, 3259–3282
4. Ghigo, A., Murabito, A., Sala, V., Pisano, A. R., Bertolini, S., Gianotti, A., et al. (2022) A PI3K γ mimetic peptide triggers CFTR gating, bronchodilation, and reduced inflammation in obstructive airway diseases. *Sci. Transl. Med.* **14**, eabl6328
5. Perino, A., Ghigo, A., Ferrero, E., Morello, F., Santulli, G., Baillie, G. S., et al. (2011) Integrating cardiac PIP3 and cAMP signaling through a PKA anchoring function of p110 γ . *Mol. Cell* **42**, 84–95
6. Lopes, J. L., Miles, A. J., Whitmore, L., and Wallace, B. A. (2014) Distinct circular dichroism spectroscopic signatures of polyproline II and unordered secondary structures: applications in secondary structure analyses. *Protein Sci.* **23**, 1765–1772
7. Newlon, M. G., Roy, M., Morikis, D., Carr, D. W., Westphal, R., Scott, J. D., et al. (2001) A novel mechanism of PKA anchoring revealed by solution structures of anchoring complexes. *EMBO J.* **20**, 1651–1662
8. d'Angelo, I., Conte, C., La Rotonda, M. I., Miro, A., Quaglia, F., and Ungaro, F. (2014) Improving the efficacy of inhaled drugs in cystic fibrosis: challenges and emerging drug delivery strategies. *Adv. Drug Deliv. Rev.* **75**, 92–111
9. Butnarusu, C., Caron, G., Pacheco, D. P., Petrini, P., and Visentin, S. (2022) Cystic fibrosis mucus model to design more efficient drug therapies. *Mol. Pharm.* **19**, 520–531
10. Boegh, M., and Nielsen, H. M. (2015) Mucus as a barrier to drug delivery - understanding and mimicking the barrier properties. *Basic Clin. Pharmacol. Toxicol.* **116**, 179–186
11. Gramegna, A., Amati, F., Terranova, L., Sotgiu, G., Tarsia, P., Miglietta, D., et al. (2017) Neutrophil elastase in bronchiectasis. *Respir. Res.* **18**, 211
12. Hobbs, C. A., Blanchard, M. G., Alijevic, O., Tan, C. D., Kellenberger, S., Bencharit, S., et al. (2013) Identification of the SPLUNC1 ENaC-inhibitory domain yields novel strategies to treat sodium hyperabsorption in cystic fibrosis airway epithelial cultures. *Am. J. Physiol. Lung Cell Mol. Physiol.* **305**, L990–L1001
13. Mall, M. A., Criner, G. J., Miravittles, M., Rowe, S. M., Vogelmeier, C. F., Rowlands, D. J., et al. (2023) Cystic fibrosis transmembrane conductance regulator in COPD: a role in respiratory epithelium and beyond. *Eur. Respir. J.* **61**, 2201307
14. Parodi, A., Righetti, G., Pesce, E., Salis, A., Tomati, V., Pastorino, C., et al. (2022) Journey on VX-809-based hybrid derivatives towards drug-like F508del-CFTR correctors: from molecular modeling to chemical synthesis and biological assays. *Pharmaceuticals (Basel)* **15**, 274
15. Mall, M. A., Mayer-Hamblett, N., and Rowe, S. M. (2020) Cystic fibrosis: emergence of highly effective targeted therapeutics and potential clinical implications. *Am. J. Respir. Crit. Care Med.* **201**, 1193–1208
16. Byrne, D. P., Omar, M. H., Kennedy, E. J., Evers, P. A., and Scott, J. D. (2022) Biochemical analysis of AKAP-anchored PKA signaling complexes methods. *Mol. Biol.* **2483**, 297–317
17. Veine, D. M., Yao, H., Stafford, D. R., Fay, K. S., and Livant, D. L. (2014) A D-amino acid containing peptide as a potent, noncovalent inhibitor of $\alpha 5\beta 1$ integrin in human prostate cancer invasion and lung colonization. *Clin. Exp. Metastasis* **31**, 379–393

18. Garton, M., Nim, S., Stone, T. A., Wang, K. E., Deber, C. M., and Kim, P. M. (2018) Method to generate highly stable D-amino acid analogs of bioactive helical peptides using a mirror image of the entire PDB. *Proc. Natl. Acad. Sci. U. S. A.* **115**, 1505–1510
19. Casey, M., Gabillard-Lefort, C., McElvaney, O. F., McElvaney, O. J., Carroll, T., Heeney, R. C., *et al.* (2023) Effect of elxacaftor/tezacaftor/ivacaftor on airway and systemic inflammation in cystic fibrosis. *Thorax* **78**, 835–839
20. Schaupp, L., Addante, A., Voller, M., Fentker, K., Kuppe, A., Bardua, M., *et al.* (2023) Longitudinal effects of elxacaftor/tezacaftor/ivacaftor on sputum viscoelastic properties, airway infection and inflammation in patients with cystic fibrosis. *Eur. Respir. J.* **62**, 2202153
21. Ibrahim, B. M., Park, S., Han, B., and Yeo, Y. (2011) A strategy to deliver genes to cystic fibrosis lungs: a battle with environment. *J. Control Release* **155**, 289–295
22. Capurro, V., Tomati, V., Sondo, E., Renda, M., Borrelli, A., Pastorino, C., *et al.* (2021) Partial rescue of F508del-CFTR stability and trafficking defects by double corrector treatment. *Int. J. Mol. Sci.* **22**, 5262
23. Graeber, S. Y., Vitzthum, C., Pallenberg, S. T., Naehrlich, L., Stahl, M., Rohrbach, A., *et al.* (2022) Effects of elxacaftor/tezacaftor/ivacaftor therapy on CFTR function in patients with cystic fibrosis and one or two F508del alleles. *Am. J. Respir. Crit. Care Med.* **205**, 540–549
24. Veit, G., Roldan, A., Hancock, M. A., Da Fonte, D. F., Xu, H., Hussein, M., *et al.* (2020) Allosteric folding correction of F508del and rare CFTR mutants by elxacaftor-tezacaftor-ivacaftor (trikafta) combination. *JCI Insight* **5**, e139983
25. Nichols, D. P., Morgan, S. J., Skalland, M., Vo, A. T., Van Dalen, J. M., Singh, S. B., *et al.* (2023) Pharmacologic improvement of CFTR function rapidly decreases sputum pathogen density, but lung infections generally persist. *J. Clin. Invest.* **133**
26. Wang, L., Wang, N., Zhang, W., Cheng, X., Yan, Z., Shao, G., *et al.* (2022) Therapeutic peptides: current applications and future directions. *Signal. Transduct. Target. Ther.* **7**, 48
27. Oriano, M., Terranova, L., Sotgiu, G., Sadri, L., Bellofiore, A., Retucci, M., *et al.* (2019) Evaluation of active neutrophil elastase in sputum of bronchiectasis and cystic fibrosis patients: a comparison among different techniques. *Pulm. Pharmacol. Ther.* **59**, 101856
28. Sharifian Gh, M. (2021) Recent experimental developments in studying passive membrane transport of drug molecules. *Mol. Pharm.* **18**, 2122–2141
29. Hermanson, G. T. (2008) *Bioconjugate Techniques*, 3rd, Academic Press, New York, NY
30. Louis-Jeune, C., Andrade-Navarro, M. A., and Perez-Iratxeta, C. (2012) Prediction of protein secondary structure from circular dichroism using theoretically derived spectra. *Proteins* **80**, 374–381
31. Hawkins, P. C., and Nicholls, A. (2012) Conformer generation with OMEGA: learning from the data set and the analysis of failures. *J. Chem. Inf. Model.* **52**, 2919–2936
32. Hawkins, P. C., Skillman, A. G., Warren, G. L., Ellingson, B. A., and Stahl, M. T. (2010) Conformer generation with OMEGA: algorithm and validation using high quality structures from the Protein Databank and Cambridge Structural Database. *J. Chem. Inf. Model.* **50**, 572–584
33. Hawkins, P. C., Skillman, A. G., and Nicholls, A. (2007) Comparison of shape-matching and docking as virtual screening tools. *J. Med. Chem.* **50**, 74–82
34. Muchmore, S. W., Souers, A. J., and Akritopoulou-Zanze, I. (2006) The use of three-dimensional shape and electrostatic similarity searching in the identification of a melanin-concentrating hormone receptor 1 antagonist. *Chem. Biol. Drug Des.* **67**, 174–176
35. Jumper, J., Evans, R., Pritzel, A., Green, T., Figurnov, M., Ronneberger, O., *et al.* (2021) Highly accurate protein structure prediction with AlphaFold. *Nature* **596**, 583–589
36. Rathinaswamy, M. K., Dalwadi, U., Fleming, K. D., Adams, C., Stariha, J. T. B., Pardon, E., *et al.* (2021) Structure of the phosphoinositide 3-kinase (PI3K) p110 γ -p101 complex reveals molecular mechanism of GPCR activation. *Sci. Adv.* **7**, eabj4282
37. Lamiable, A., Thevenet, P., Rey, J., Vavrusa, M., Derreumaux, P., and Tuffery, P. (2016) PEP-FOLD3: faster *de novo* structure prediction for linear peptides in solution and in complex. *Nucleic Acids Res.* **44**, W449–W454
38. Wang, Z., Eickholt, J., and Cheng, J. (2011) APOLLO: a quality assessment service for single and multiple protein models. *Bioinformatics* **27**, 1715–1716
39. Corpora, T., Roudaia, L., Oo, Z. M., Chen, W., Manuylova, E., Cai, X., *et al.* (2010) Structure of the AML1-ETO NHR3-PKA(RII α) complex and its contribution to AML1-ETO activity. *J. Mol. Biol.* **402**, 560–577
40. Vangone, A., Schaarschmidt, J., Koukos, P., Geng, C., Citro, N., Trellet, M. E., *et al.* (2019) Large-scale prediction of binding affinity in protein-small ligand complexes: the PRODIGY-LIG web server. *Bioinformatics* **35**, 1585–1587
41. Xue, L. C., Rodrigues, J. P., Kastritis, P. L., Bonvin, A. M., and Vangone, A. (2016) PRODIGY: a web server for predicting the binding affinity of protein-protein complexes. *Bioinformatics* **32**, 3676–3678